J. Fluid Mech. (2005), *vol.* 530, *pp.* 181–195.
doi:10.1017/S002211200500354X Printed in the United Kingdom

Bubble formation in a coflowing air–water stream

By A. SEVILLA, J. M. GORDILLO† AND C. MARTÍNEZ-BAZÁN

Área de Mecánica de Fluidos, Departamento de Ingeniería Térmica y de Fluidos, Universidad Carlos III de Madrid, Avda. de la Universidad 30, 28911, Leganés (Madrid), Spain

(Received 1 August 2003 and in revised form 29 November 2004)

In this work, we present a detailed experimental study of the periodic formation of bubbles in an air–water coflowing stream, as well as a simple model to describe the process. The frequency of formation of bubbles was measured analysing a large number of images recorded with a high-speed camera for a wide range of experimental conditions and air-injection needle geometries. The analysis of the images indicated that the bubble-formation process consisted of two distinct stages, namely the *ligament expansion stage*, characterized by the radial growth of an air ligament left attached to the injection needle after the pinch-off of a bubble, and the *ligament collapse stage*, characterized by the formation of a neck at the tip of the injection needle which propagates downstream, at a velocity which is nearly the liquid velocity, until it collapses generating a new bubble. A simplified model, based on the Rayleigh–Plesset equation for a cylindrical geometry to determine the dynamics of the liquid stream and on Bernoulli's equation to determine the air pressure near the neck, has been proposed to estimate the duration of the ligament collapse stage, t_{col}. The experimental bubble-formation frequency, properly scaled with the breakup time given by the model, is shown to collapse onto the same curve for all the experimental conditions used here, indicating that our simple model seems to retain the main physical aspects of the process.

1. Introduction

Generation of foams and bubbles has become an area of major importance for an increasing number of industrial processes such as in water treatment, metallurgy and the chemical industry among others. Recently, production of foams formed with a uniform size distribution of micro-bubbles has been an active research area in material science (Gibson & Ashby 1999) and the food industry. In particular, in the case of the chemical industry, micron-sized bubbles are desired to increase the surface to volume ratio. A commonly used mechanism to produce bubbles is to place a gas injection needle coaxially into a liquid jet. Thus, the size of the bubbles generated is decreased compared to the case without coflow (Chuang & Goldschmidt 1970; Oğuz & Prosperetti 1993).

There are different theoretical approaches to describe the process of bubble generation from a needle. For instance, Kumar & Kuloor (1970), Chuang & Goldschmidt (1970) and Bhunia *et al.* (1998), among others, provided models for

† Present address: Escuela Superior de Ingenieros, Universidad de Sevilla, Camino de los Descubrimientos s/n, 41092 Sevilla, Spain.

bubble formation based on force balances assuming a spherical growth of the bubble. Other authors performed temporal stability analysis of the coflowing gas–liquid jet configuration without including any experimental evidence, i.e. Parthasarathy & Chiang (1998). A more detailed analysis, which accounts for the convective or absolute nature of the instabilities can be found in Gordillo, Gañán Calvo & Pérez-Saborid (2001). In this work, the periodic bubble formation is associated with the existence of an absolute instability caused either by capillary effects or by density effects previously described by Monkewitz & Sohn (1988) as a *hot-jet* instability. Furthermore, Sevilla, Gordillo & Martínez-Bazán (2002) performed a spatio-temporal stability analysis of coflowing streams with different densities and velocities where the effect of the outer mixing layer that develops between the coflowing liquid stream and the surrounding quiescent liquid was included. Their analysis revealed that the nature of the instability was convective under the conditions for which long liquid–liquid coflowing jets were experimentally observed. On the other hand, for gas–liquid coflowing jets, where periodic bubble formation is commonly observed, the nature of the instability was absolute. Consequently, under the point of view of the stability analysis, the periodic formation of bubbles has been related to the existence of an absolute instability.

The physical mechanisms of bubble formation under well-defined experimental conditions were described by Oğuz & Prosperetti (1993). In this study, the authors performed a detailed comparison between experimental measurements and numerical calculations of the bubble growth and detachment from a needle, showing an excellent agreement between both results. This study also revealed the role of the liquid coflow in decreasing the bubble size and demonstrated the importance of the viscous pressure drop inside the needle to control the bubble volume.

In the present work, we study the bubble-formation process inside a coflowing stream under conditions different from those found in the literature. The different situations explored here permitted us to identify two distinct stages in the bubble generation process that, to our knowledge, have never been reported before, and clarify the importance of the unsteady motion of the gas inside the injection needle during the process. One of the main characteristics of this study is that, since we will focus on the bubble formation in a coflowing water jet discharging into a stagnant air atmosphere, buoyancy effects will be negligible. In addition, as will be described later in the paper, our experimental set-up avoids the influence of an outer liquid–liquid shear layer present in other related experiments and whose influence was already documented by Sevilla *et al.* (2002). It must be mentioned that the experimental set-up employed in our study is similar to that used by Kendall (1986), where the formation of liquid shells was described. The main difference with Kendall's flow configuration is that we focus on larger outer liquid to inner gas diameter ratios, a feature that completely changes the bubble-formation mechanisms.

The paper is organized as follows. In § 2, we describe the experimental set-up and the experimental results will be presented in § 3. A simplified theoretical model that explains the physics involved in the bubble-generation process is presented in § 4. Finally, § 5 is devoted to the conclusions.

2. Experimental set-up

The facility, shown in figure 1, consisted of a nozzle of radius $r_w = 3\,\mathrm{mm}$ which provided a jet of water discharging upwards into a still air atmosphere. A uniform water velocity profile was achieved at the exit of the nozzle by using a perforated plate upstream of a high contraction nozzle of area ratio 70:1. An air stream was injected

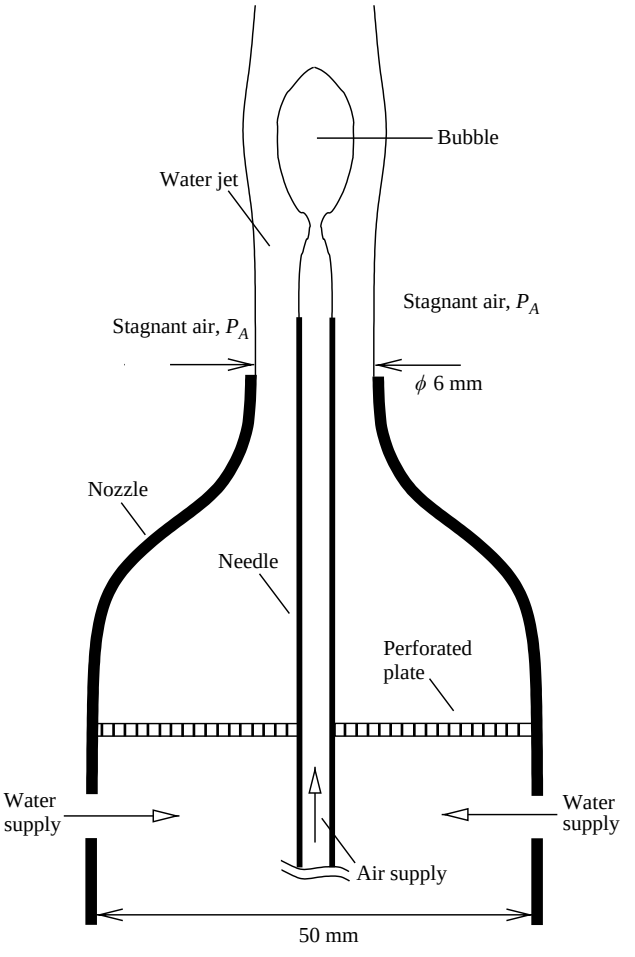

FIGURE 1. Detail of the water nozzle and air injection system.

at the centreline of the water jet with a stainless steel hypodermic needle. To avoid possible perturbations in the bubble-formation process, generated by imperfections in the water nozzle, the tip of the needle was located at approximately half a diameter downstream from the exit of the water nozzle. In all the experiments reported here, the water nozzle employed was the same and we used different needles to vary the diameter and the length of the air injection tube. The geometrical characteristics of the different needles employed, hereinafter named needles I, II*a*, II*b* and III, are summarized in table 1 where r_i, r_o are the inner and outer radii, respectively, and l_t is the length of the needle. Needle II*b*, whose inner and outer radii are the same as those of needle II*a* and whose length is twice as long as that of needle II*a*, was used to study the possible effect of the needle length on the bubble-formation process. A schematic representation of the geometrical parameters of the problem at the breakup point can be found in figure 2, where r_a is the radius of the air ligament, r_w is the water jet radius, l_i is the length of the air intact ligament and l_b is the length of the bubble. In most of the experiments reported here r_a was equal to r_o.

The water flow was supplied from a constant-pressure bladder tank, while the air flow, supplied from a pressurized chamber to the injection needle through a 3 m long

Needle	r_i(mm)	r_o(mm)	l_t/r_i	r_w/r_o
I	0.597	0.8255	410	3.6
II*a*	0.419	0.635	573	4.7
II*b*	0.419	0.635	1396	4.7
III	0.292	0.451	736	6.6

TABLE 1. Geometrical properties of the four different needles used in the experiments. Here, r_i and r_o are the inner and outer radius of the air injection needle, respectively, l_t is the length of the needle and r_w is the radius of the water jet.

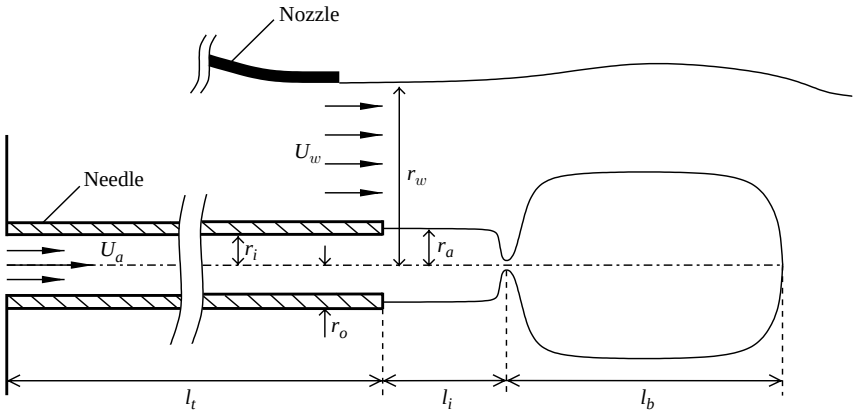

FIGURE 2. Sketch of the air intact ligament and growing bubble indicating the geometrical parameters. Here, r_w is the radius of the water jet, r_a is the radius of the air ligament, r_o and r_i are the outer and inner radii of the injection needle, l_t is the length of the needle, l_i the length of the air intact ligament and l_b the length of the bubble.

pipe, was controlled with a pressure regulator and a high-precision valve. Since, at the exit of the needle, the pressure fluctuations caused by the breakage of a bubble are very small compared to the pressure drop across the high-resolution valve, the air supply system ensures a constant flow rate of air. The water flow rate, Q_w, was varied from $Q_w = 5 \times 10^{-5}$ m^3 s^{-1} to $Q_w = 1.6 \times 10^{-4}$ m^3 s^{-1}. Therefore, the water jet velocity, calculated by dividing the flow rate by the corresponding exit cross-section $U_w = Q_w/(\pi(r_w^2 - r_o^2))$, varied from $U_w = 1.85$ m s^{-1} to $U_w = 9.65$ m s^{-1} giving Reynolds numbers $11\,100 < Re_w = 2\,U_w\,r_w/\nu < 57\,900$ where ν is the kinematic viscosity of water. Similarly, the air flow rate, Q_a, was varied from $Q_a = 5 \times 10^{-7}$ m^3 s^{-1} to $Q_a = 2.8 \times 10^{-5}$ m^3 s^{-1} giving a range of air velocities of 2.72 m s^{-1} $< U_a = Q_a/(\pi r_i^2) <$ 58.49 m s^{-1}, and Reynolds numbers $115 < Re_a = 2\,Q_a/(\pi\,r_i\,\nu_a) < 1770$ where ν_a is the kinematic viscosity of air. Finally, measurements were performed by uniformly illuminating the measuring area with a white bulb light, and by recording images of the time evolution of the air–water coaxial jet with a Kodak Motion Corder Analyzer high-speed camera whose maximum display size was 512×480 at recording rates up to 250 frames per second (f.p.s.). Higher recording rates could be obtained by reducing the resolution. Thus, in the experiments reported here, the images were taken at a rate which varied from 2000 f.p.s. with a resolution of 256×120 to 5000 f.p.s. with a pixel resolution of 128×120, with a shutter speed of 5×10^{-5} s.

In the present work, the water-jet Reynolds number was sufficiently large to enable us to neglect viscous effects in the water stream. Moreover, although the large values

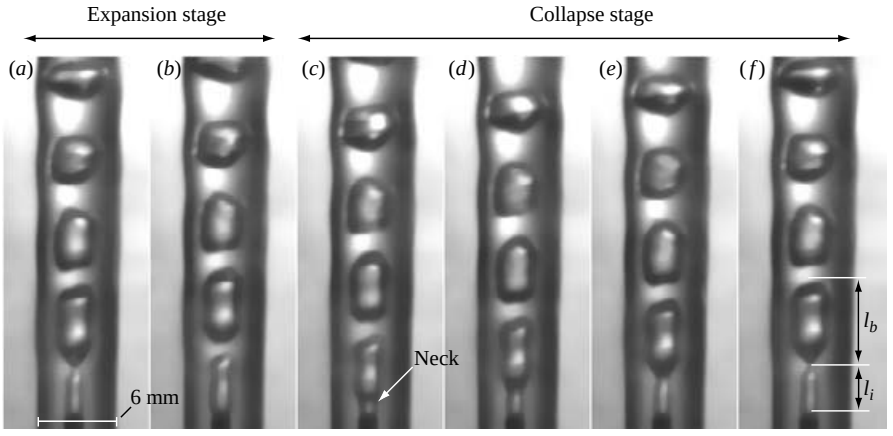

FIGURE 3. Time evolution of the bubble-formation process. Injection needle II*b*, $U_a = 18.43\,\mathrm{m\,s^{-1}}$, $U_w = 2.5\,\mathrm{m\,s^{-1}}$. The spatial resolution of the images is 9 pixels $\mathrm{mm^{-1}}$ and the interval of time between frames is $\Delta t = 5 \times 10^{-4}$ s.

of air Reynolds number Re_a indicate that viscous effects are negligible within the bubble, the flow inside the needle is a fully developed laminar flow. In addition, the Froude number, $Fr = gr_o/U_w^2$, was very small and, therefore, the control parameters of the air breakup process reduced to the air Weber number, $We = \rho_a(U_a - U_w)^2 r_o/\sigma$ where ρ_a denotes the air density and σ the surface tension coeficient, which varied from 0.08 to 18, the water-to-air velocity ratio, U_w/U_a, with $U_w/U_a < 0.5$, and the geometrical parameters, namely the water-to-air diameter ratio, r_w/r_o, the ratio of the outer to inner needle radius, r_o/r_i, and the needle length to inner radius ratio, l_t/r_i.

3. Experimental results

In this section, we will describe the bubble-generation process observed from images captured with a high-speed camera at recording rates which varied from 2000 f.p.s. to 5000 f.p.s. Thus, we will deduce the different mechanisms leading to the formation of bubbles and we will identify the dominant forces which control the bubbling frequency using physical arguments based on our observations.

A sequence of six consecutive pictures corresponding to the formation of a bubble using needle II*a*, $U_a = 18.43\,\mathrm{m\,s^{-1}}$ and $U_w = 2.5\,\mathrm{m\,s^{-1}}$, is shown in figure 3. In this sequence, the time interval between two consecutive frames was $\Delta t = 5 \times 10^{-4}$ s. The bubble-formation process can be briefly described as follows. After a bubble pinches-off from the tip of the needle (figure 3*a*) there is an air ligament, of diameter approximately equal to the outer needle diameter, that remains attached to the needle. The air ligament will be called hereinafter the *intact ligament* and its length, l_i, will be denoted the *intact length*. Immediately after the bubble separates, the intact ligament starts to grow radially while it propagates downstream. It can also be observed that, after a certain interval of time, a neck appears in the air stem at the needle tip (figure 3*b*). Notice that, between the pinch-off of a bubble and the formation of the neck, the intact ligament expands radially. Thus, this period of time of duration t_{exp} will be named the *ligament expansion stage*. Once the ligament expansion stage finishes, the neck propagates downstream while its diameter decreases until the air stem eventually breaks, thereby forming a new bubble at the end of the intact ligament (see figure 3*c–f*). The lapse of time, of duration t_{col}, that separates the formation of the

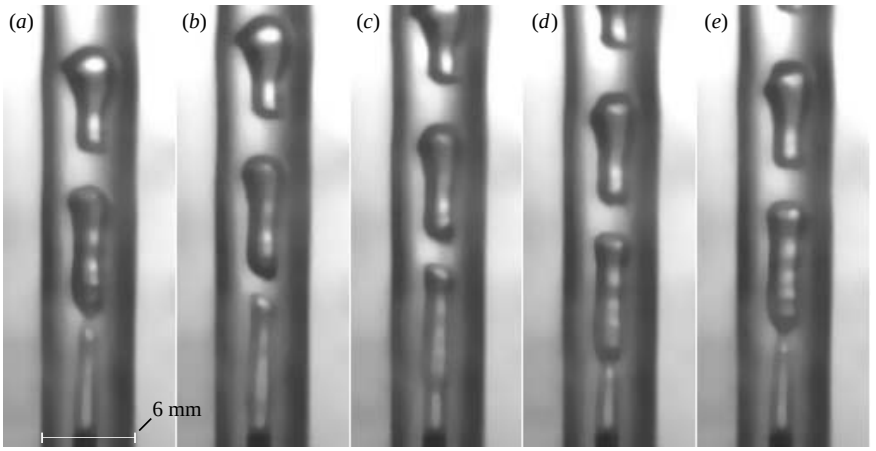

FIGURE 4. Time evolution of the bubble-formation process. Injection needle II*b*, $U_a = 18.43\,\mathrm{m\,s^{-1}}$, $U_w = 4.3\,\mathrm{m\,s^{-1}}$. The spatial resolution of the images is 9 pixels $\mathrm{mm^{-1}}$ and the interval of time between frames is $\Delta t = 5 \times 10^{-4}$ s.

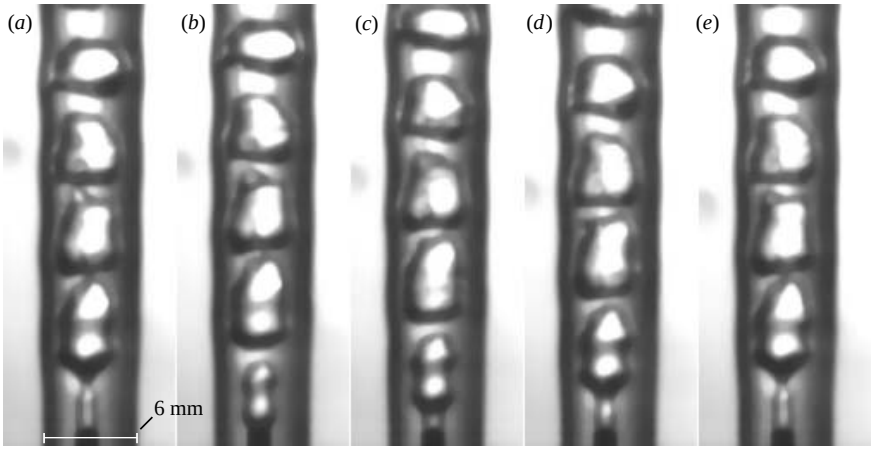

FIGURE 5. Time evolution of the bubble-formation process. Injection needle II*b*, $U_a = 28.41\,\mathrm{m\,s^{-1}}$, $U_w = 2.5\,\mathrm{m\,s^{-1}}$. The spatial resolution of the images is 9 pixels $\mathrm{mm^{-1}}$ and the interval of time between frames is $\Delta t = 5 \times 10^{-4}$ s.

neck from the pinch-off of the following bubble will be named the *ligament collapse stage* (figure 3*c–f*). During the ligament collapse stage, the bubble joined to the tip of the intact ligament keeps expanding radially. Notice that in figures 3(*a*) and 3(*f*), the end of the ligament collapse stage coincides with the beginning of the expansion stage and, consequently, the process is fully periodic. Thus, the time a bubble takes to form will be denoted $t_b = t_{exp} + t_{col} = 1/f_b$, where f_b is simply the bubbling frequency. At this point, it must be mentioned that we have restricted our study to values of the velocity ratio smaller than 0.5, since our observations demonstrated that, under certain conditions, the process was no longer periodic for $U_w/U_a \gtrsim 0.5$ (see Sevilla, Gordillo & Martínez-Bazán 2005).

Figures 4 and 5 show how the bubble-generation process varies with U_a and U_w. For example, figure 4 exhibits the formation of a bubble under the same experimental conditions as those given in figure 3, but with higher water velocity. It must be noticed

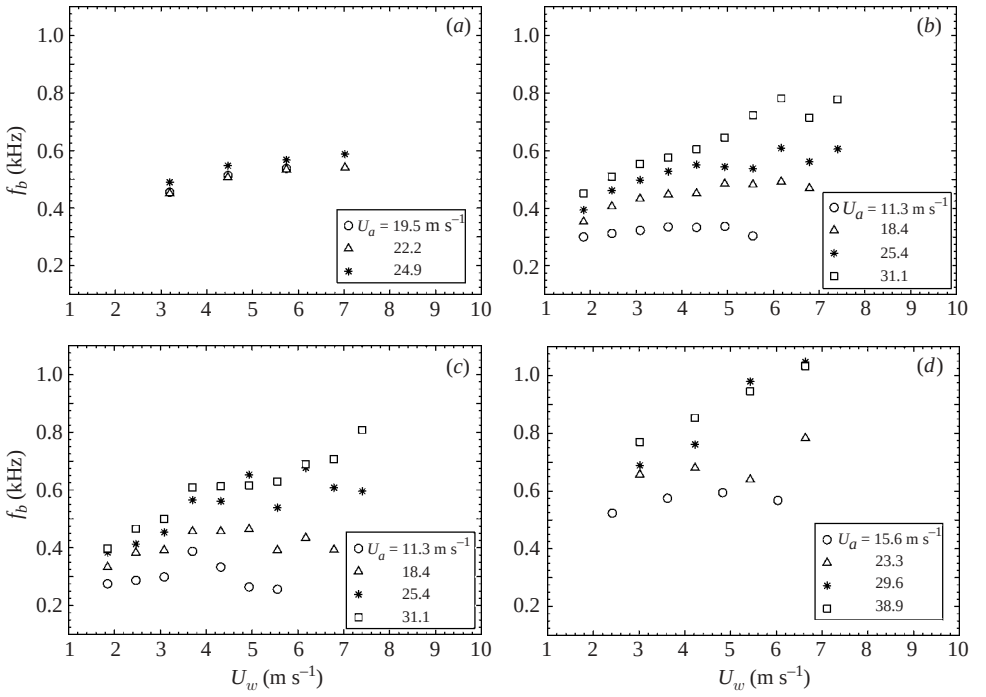

FIGURE 6. Dependence of the bubble break-up frequency on the liquid velocity for different values of the air injection velocity. (*a*) Needle I, (*b*) needle II*a*, (*c*) needle II*b*, (*d*) needle III.

that, when U_w increases, the length of the intact ligament increases, the bubble diameter decreases and the ligament expansion stage, t_{exp}, is shortened. Similarly, figure 5 shows the formation process of a bubble under the same conditions as those given in figure 3, but with higher air velocity. Note that the effect of increasing U_a, keeping U_w constant, is qualitatively opposed to that observed in figure 4.

The bubble-generation frequency, calculated by counting thge number of bubbles formed during a large recording time, is depicted in figure 6 for some of the experiments performed here. This figure shows the qualitative trend of the bubbling frequency with the water and the air velocities. Note that the frequency increases with the air velocity when the water velocity remains constant. Alternatively, it can also be observed that the frequency does not vary monotonically with the water velocity when the air velocity remains constant. In addition, the time evolution of the gas volume injected into the water stream was also determined measuring the volume of air in each frame through the use of image analysis, and plotted in figure 7 for three consecutive bubbles. An important conclusion that can be extracted from this figure is that, since the time evolution of the volume is practically linear during the whole bubble-formation period, the air flow rate remains nearly constant during the process. Thus, the measurements confirm that our experimental set-up ensures a nearly constant flow rate of air during most of the bubble-formation process.

We will now proceed to deduce the mechanisms underlying the bubble-formation process in the following subsection.

3.1. *Qualitative explanation of the ligament expansion and collapse stages*

Coming back to figure 3, it can be observed that during the ligament collapse stage (figure 3*c–f*), the air stream exiting the needle remains parallel to the needle outer

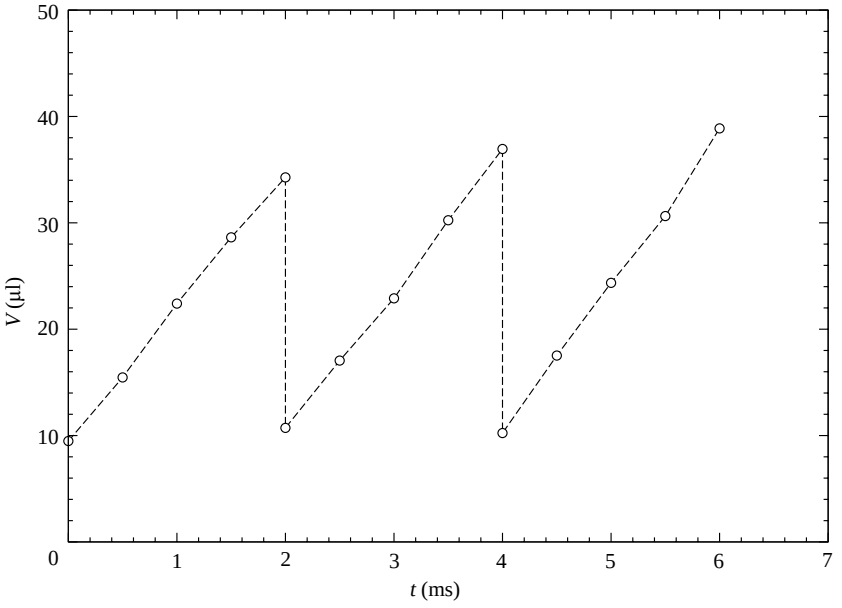

FIGURE 7. Time evolution of the volume of a forming bubble. Notice that, since the volume increases linearly with time, the flow rate of air remains nearly constant during the process.

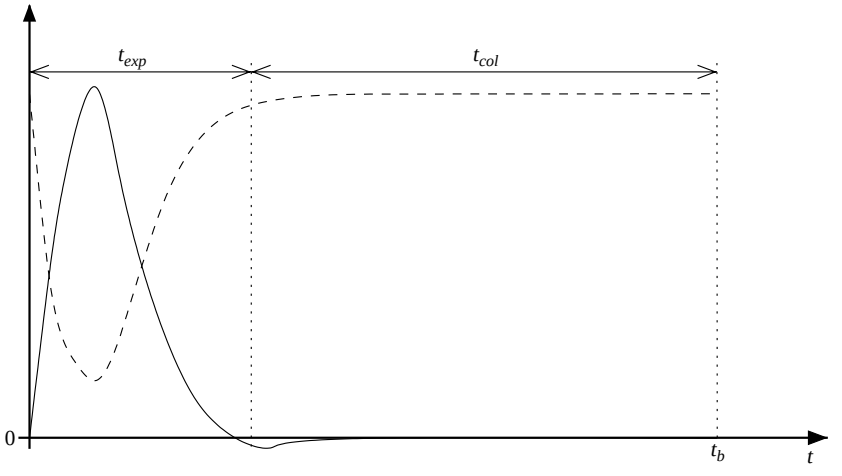

FIGURE 8. Sketch of the time evolution of the pressure (solid line), $p_e - P_A$ and air flow rate at the exit of the needle (dashed line), q_e.

surface. This observation suggests that, neglecting surface tension effects, the air flow discharges into the liquid jet at ambient pressure, P_A, during the time interval from figures 3(*c*) to (3*f*). Alternatively, during the ligament expansion stage (figures 3*a*–3*b*) the air stem inflates very quickly, suffering an important outward radial acceleration. Such radial acceleration implies that, during part of this stage, the pressure inside the air ligament must be higher than the ambient pressure. Consequently, the qualitative time evolution of the gas pressure, $p_e - P_A$ and the air flow rate, q_e, at the exit of the injection needle during a bubble-formation period can be sketched as shown in figure 8. Note that during a small fraction of time the exit gas flow rate, q_e, must

Needle	*We*	U_w/U_a	Δp_a (Pa)	Δp_i (Pa)	Δp_c (Pa)
I	4.78	0.17	1923	138	6241
I	5.47	0.16	1923	162	6766
I	6.34	0.15	1649	193	7383
I	7.08	0.14	1141	220	7877
I	7.91	0.14	1966	250	8402
I	8.94	0.13	2473	288	9019
II*a*	10.72	0.06	5405	517	12 080
II*a*	7.13	0.12	4054	312	9374

TABLE 2. Comparison between the estimated value of the maximum pressure inside the air stem, Δp_a, and the different mechanisms of increase in pressure.

decrease owing to the gas deceleration caused by the increase of the exit pressure, p_e. This observation was experimentally verified by measuring the pressure at the entrance of the needle with and without a coaxial water flow for the same values of the air flow rate. Our measurements confirmed that the mean entrance pressure was slightly higher when a jet of water was injected coaxially into the air jet than that obtained without water coflow. However, as shown in figures 3–5, the interval of time for which $p_e > P_A$ is only a small fraction of the bubbling time, indicating that the average exit pressure can be considered to be nearly equal to P_A.

To determine the cause of the rapid growth of the bubble during the ligament expansion stage, we have estimated in table 2 the different sources of the increase in pressure inside the air ligament. In this table, $\Delta p_a \sim \rho_w r_o \ln(r_w/r_o)\Delta v/\Delta t$, where Δv is the increment of radial velocity in a time interval Δt, is the overpressure during the ligament expansion stage calculated from estimates of the air ligament radial velocity performed by measuring the time evolution of the interface from the images recorded. On the other hand, $\Delta p_i \sim (1/2)\rho_a (U_a - U_w)^2$ denotes the gas overpressure caused by the incompressible deceleration of the air stream from the initial velocity at the exit of the needle to the axial velocity of the bubble interface, which is approximately equal to the surrounding liquid velocity, and $\Delta p_c = \rho_a c (U_a - U_w)$ is the overpressure produced by a rapid pinch-off of a bubble from the intact ligament (similar to what happens in the water-hammer phenomenon due to the sudden closure of a valve in a pipe). To estimate Δp_c, we took into account the fact that the rapid closure of the neck, occurring when a bubble pinches-off from the air ligament, leads to a compression wave which raises the pressure to values of the order of $\rho_a c (U_a - U_w)$. However, the values of Δp_c shown in table 2 have been calculated assuming a perfectly rigid medium surrounding the gas and, therefore, they have been overestimated. Furthermore, the recording rate of our images was smaller than that required to resolve the expansion stage properly and, consequently, the values of Δp_a have been underestimated. Nevertheless, table 2 clearly shows how purely incompressible mechanisms cannot cause the initial radial accelerations observed in the flow, and compressibility effects must be considered during the ligament expansion stage. At the final instants of the ligament expansion stage, the increasing volume growth-rate of the air ligament, q_e, causes the exit overpressure, $p_e - P_A$ to decrease (see figure 8) until the end of the expansion stage where $p_e = P_A$. In effect, note that q_e increases while the liquid keeps accelerating radially outwards or, similarly, while $p_e > P_A$. The ligament expansion stage finishes with the formation of a neck in the air stem at the needle tip, giving birth to the ligament collapse stage. Notice that the

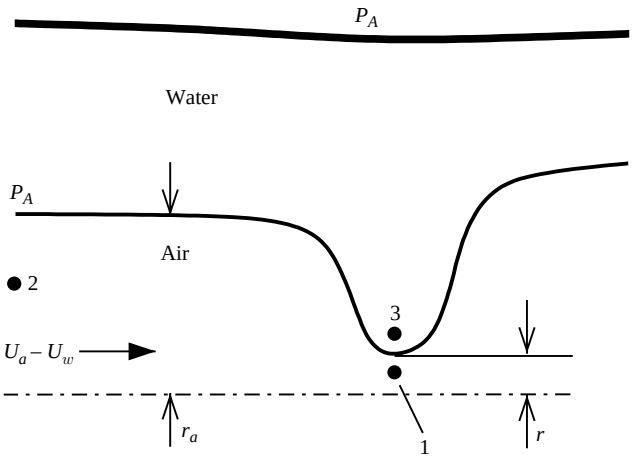

FIGURE 9. Detail of the air ligament and the region near the neck before pinching-off in a frame of reference moving with the neck velocity U_w. The air flow enters the ligament with a relative velocity $U_a - U_w$. Here, 1 represents a point inside the neck in the air stream, 2 is a point at the exit of the needle and 3 is a point in the liquid stream surrounding the neck.

formation of the neck requires that the exit pressure is lower than, or equal to P_A. Consequently, in our simplified description, we will assume that the ligament collapse stage starts when $p_e = P_A$ ($q_e = Q_a$). This latter condition states that after finishing the ligament expansion stage, p_e becomes smaller than P_A and the liquid surrounding the needle tip starts to move radially towards the axis, generating a neck (see figures 3*c* and 8). Thus, we can conclude that the neck is formed at the end of the ligament expansion stage because the pressure difference between the outer (water) and the inner (air) streams, $P_A > p_e$, forces the water–air interface to move radially toward the axis. An important point is that the expansion time and, consequently, the period of time where both the pressure and the flow rate at the exit of the injection needle are different from their respective mean values, is very small compared to the bubbling time and, therefore, we can assume that the flow rate remains constant during the ligament collapse stage.

In conclusion, in this section we have explained the occurrence of both the ligament expansion and collapse stages. The following section will be devoted to quantifying the characteristic time scale involved in the ligament collapse stage, with the aim of providing the correct scaling for the bubbling frequency.

4. Scaling of the bubble-formation frequency

The model developed to describe the ligament collapse stage is based on the assumption that the gas flow rate supplied by the needle remains constant and equal to $Q_a = \pi r_i^2 U_a$ during this stage. Another essential aspect is that, as suggested by figures 3–5, the intact ligament can be modelled by a cylinder of constant radius r_o with a contraction at the neck region (see figures 2 and 3*f*). To estimate the collapse time it is necessary to know the air pressure inside the neck region. This pressure can be calculated by applying Bernoulli's equation between points 1 and 2 of figure 9 in a frame of reference moving with the velocity of the neck, which is assumed to be equal to the liquid velocity U_w. This approximation, already mentioned in the previous sections, was based on our experimental measurements of the trajectory of the neck,

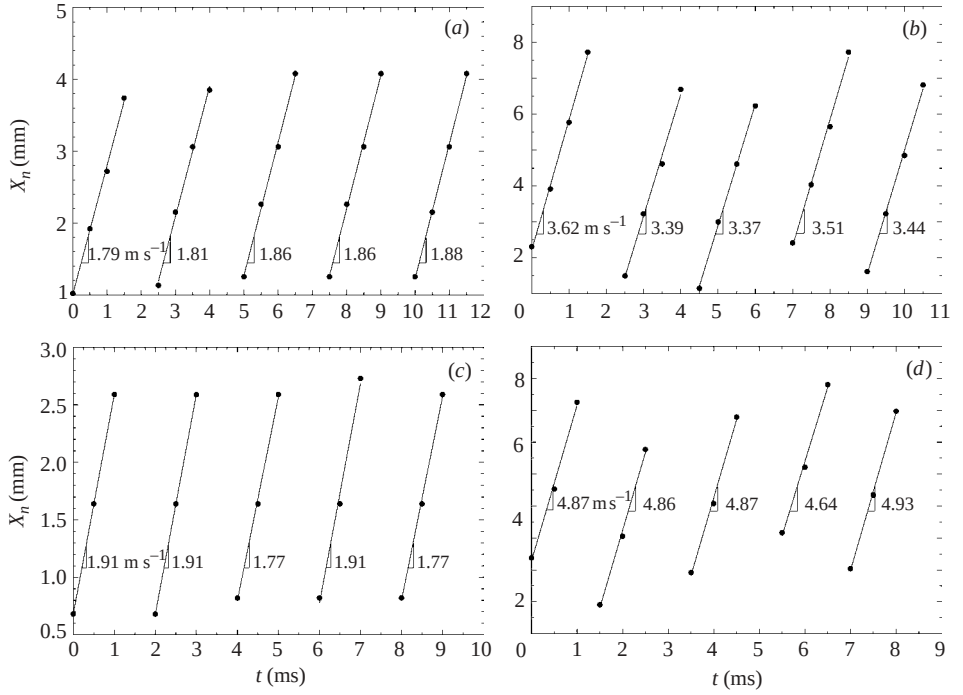

FIGURE 10. Time evolution of the position of the neck, x_n, for different values of U_w and U_a. (*a*) $U_a = 18.4\,\mathrm{m\,s^{-1}}$, $U_w = 2.47\,\mathrm{m\,s^{-1}}$, (*b*) $U_a = 18.4\,\mathrm{m\,s^{-1}}$, $U_w = 4.32\,\mathrm{m\,s^{-1}}$, (*c*) $U_a = 28.4\,\mathrm{m\,s^{-1}}$, $U_w = 2.47\,\mathrm{m\,s^{-1}}$, (*d*) $U_a = 18.4\,\mathrm{m\,s^{-1}}$, $U_w = 6.17\,\mathrm{m\,s^{-1}}$. Observe that the velocity of the neck ranges from 0.75 to 0.8 times the water velocity.

$x_n(t)$, performed for different values of U_w and U_a. Some of the measurements are shown in figure 10 where the air-to-water velocity ratio ranges from 0.09 to 0.33. Notice that, although the velocity of the neck is slightly smaller than U_w, it is always approximately equal to 80 % of the water velocity independently of U_w/U_a. Thus, to simplify the model we considered that the neck always propagated at U_w.

Since, when the air ligament exits parallel to the needle, the pressure of the water surrounding the air stream is P_A,

$$P_2 = P_A + \frac{\sigma}{r_o}. \tag{4.1}$$

Consequently,

$$P_1 = P_A + \frac{\sigma}{r_o} + \tfrac{1}{2}\,\rho_a\,(U_a - U_w)^2\left[1 - \left(\frac{r_o}{r}\right)^4\right], \tag{4.2}$$

and the pressure of the water surrounding the neck (point 3) can be approximated by $P_3 \simeq P_1 - \sigma/r$, where $r(t)$ is the instantaneous radius of the neck. The positive radial difference of pressure $(P_A - P_3)$ accelerates the water towards the axis, producing the collapse of the neck. Once $(P_A - P_3)$ is known, the collapse time, t_{col}, can be estimated with a simple model able to describe the real process retaining the main physical aspects of the neck collapse. The approach we propose here is to model the neck as a cylinder and to use the cylindrical Rayleigh–Plesset equation to describe the dynamics

of the liquid around it. Thus,

$$(\ddot{r}\, r + \dot{r}^2) \ln \frac{r_w}{r} + \tfrac{1}{2}\dot{r}^2 r^2 \left(\frac{1}{r_w^2} - \frac{1}{r^2} \right) = \frac{\Delta P_{col}}{\rho_w}, \tag{4.3}$$

where ρ_w is the water density and

$$\Delta P_{col} = P_3 - P_A = \tfrac{1}{2}\, \rho_a\, (U_a - U_w)^2 \left[1 - \left(\frac{r_o}{r} \right)^4 \right] + \frac{\sigma}{r_o} \left(1 - \frac{r_o}{r} \right). \tag{4.4}$$

Although (4.3) could be solved with appropriate boundary conditions, our purpose here is simply to deduce the relevant time scale of the ligament collapse stage. Though the final stages of the break-up process are nonlinear, many examples in the literature of liquid atomization show that the experimental observations are predicted well by linear stability analysis (Kalaaji *et al.* 2003). This agreement is due to the fact that the time required for the perturbation to grow during the linear part of the process is much larger than the nonlinear final stages of the liquid drop pinch-off. Thus, we propose to apply the same idea to our case and linearize (4.3) around $r = r_o$, $\dot{r} = 0$ to give

$$\rho_w\, r_o^2\, \ddot{\epsilon}\, \ln \frac{r_w}{r_o} = \rho_a\, (U_a - U_w)^2\, (2 + We^{-1})\, \epsilon, \tag{4.5}$$

where $r = r_o(1 - \epsilon)$. Thus, the time scale for the collapse stage yields,

$$t_0 = \left[\ln \left(\frac{r_w}{r_o} \right) \frac{\rho_w}{\rho_a} \right]^{1/2} \frac{r_o}{(U_a - U_w)\,(2 + We^{-1})^{1/2}}. \tag{4.6}$$

Defining the dimensionless time $\tau = t/t_0$, the solution of (4.5) depends on the rest of the dimensionless parameters of the problem only through the initial conditions. Note that the characteristic time given in (4.6) could have also been obtained with a temporal stability analysis, whose detailed description can be found in the Appendix.

Considering that the ligament expansion stage is much shorter than the ligament collapse stage, $t_{exp} \ll t_{col}$, we can define a Strouhal number based on t_0 as $St_b = 2\, t_0\, f_b$. The defined Strouhal number has been plotted in figure 11 as a function of the water-to-air velocity ratio for all the experiments performed here. Note the collapse of all the experimental points onto the same curve, indicating that the time scale proposed here is, in fact, the correct one. Also notice that, for $U_w/U_a > 0.2$, the Strouhal number is approximately constant, with $St_b \simeq 1$, whereas $St_b \simeq 0.3 + 3\, U_w/U_a$ for $U_w/U_a < 0.2$. This dependence of the Strouhal number on the velocity ratio can be qualitatively explained in terms of the time needed for the neck to form. In effect, notice that St_b takes a constant value for $U_w/U_a > 0.2$, indicating that the bubbling time is only determined by the ligament collapse stage. However, as the velocity ratio decreases, t_{exp} becomes non-negligible, explaining, therefore, the dependence of the Strouhal number on the velocity ratio for $U_w/U_a < 0.2$.

In this section, we have provided a simple model to estimate the ligament collapse. The Strouhal number based on the characteristic collapse time is an order unity function of U_w/U_a, which confirms that the bubble pinch-off is due to the gas pressure drop produced by the combined action of the capillary forces and the gas convective acceleration at the neck. Given the simplifications involved in the model, most notably the condition $p_e = P_A$ used to identify the end of the ligament expansion stage, our description can only qualitatively explain the dependence of the Strouhal number on the velocity ratio U_w/U_a. Numerical simulations of the neck-formation

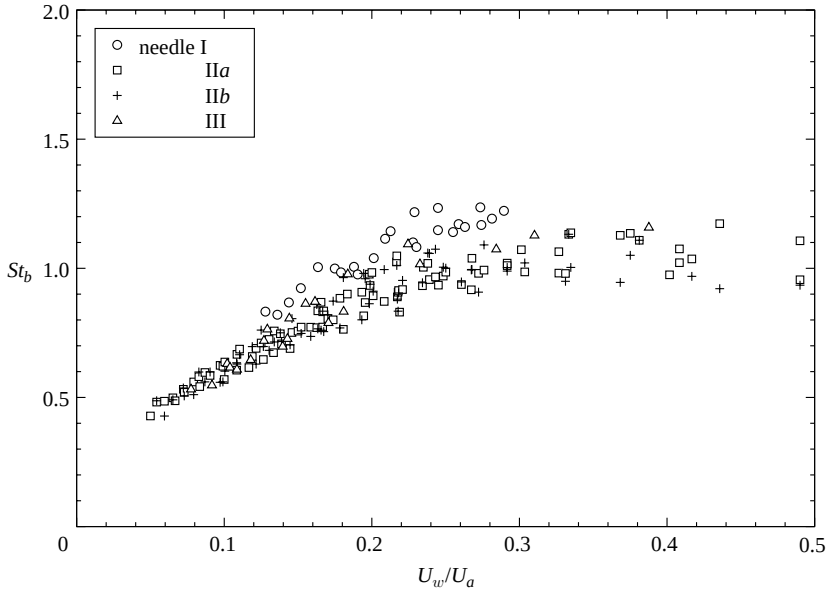

FIGURE 11. Evolution of the dimensionless bubble formation frequency, St_b, with the water-to-air velocity ratio.

process, accounting for the dynamics of the liquid stream, would be required to determine precisely both the ligament expansion and neck-formation times.

5. Conclusions

We have performed controlled experiments of bubble formation in a co-flowing air–water stream under conditions of negligible buoyancy and negligible viscous effects. A regime of periodic bubble formation has been shown to exist for values of the water-to-air velocity ratio $U_w/U_a < 0.5$. In this *bubbling regime*, there is a periodic release of air bubbles at a certain distance from the needle tip, l_i, with a frequency, f_b, whose value has been experimentally measured. Flow visualizations using a high-speed camera suggested dividing the bubble-formation process into two different stages, namely the *ligament expansion stage* followed by the *ligament collapse stage*, which starts with the formation of a neck at the needle tip.

The ligament expansion stage begins when a bubble detaches from the air stream, leaving behind an intact air ligament of length l_i, which immediately starts to grow radially, while it remains attached to the injection needle. Afterwards, the ligament expansion stage is followed by the ligament collapse stage whose duration, t_{col}, has been estimated using the linearized cylindrical Rayleigh–Plesset equation to describe the water flow surrounding the air stem and Bernoulli's equation for the air flow inside the needle. The comparison between the expansion and collapse times showed that $t_{exp}/t_{col} < 1$ in all the experiments performed, thereby suggesting the definition of the Strouhal number $St_b = 2\,t_0\,f_b$ to properly scale the bubble-formation frequency.

The proposed scaling has been checked by plotting the Strouhal number St_b versus the water-to-air velocity ratio, U_w/U_a, for a wide range of experimental conditions and several needle geometries. The collapse of all the experimental data onto the same curve indicates that the proposed model retains the essential features of the ligament collapse process. Such evidence confirms that the bubble pinch-off is caused by the

decrease of the gas pressure produced by the combined action of capillary effects and the air convective acceleration at the neck. As already explained above, our simplified description can only qualitatively describe the Strouhal-number dependence on the velocity ratio U_w/U_a, and numerical simulations would be required to determine precisely the time required for the neck to form.

Finally, it has to be pointed out that, to our knowledge, the description of the bubble-formation process presented in this paper is original in the sense that the frequency is estimated as the collapse time of the neck. This study reveals that the inertia of the gas is essential to understanding the bubble formation mechanisms. Thus, our approach is significantly different from that followed in other related works such as Kumar & Kuloor (1970), Chuang & Goldschmidt (1970) or Oğuz & Prosperetti (1993) among others, where the bubble detachment was imposed as an *ad hoc* condition.

This work has been supported by the Spanish MCyT under Project DPI2002-04550-C07. The authors would like to thank Professor F. J. Higuera for fruitful discussions.

Appendix. Scaling of the ligament collapse stage using linear stability analysis

Let us consider the temporal stability analysis of Kelvin–Helmholtz type (uniform basic velocity profiles) moving in a frame of reference at the liquid velocity. Denoting $(\bar{u}_{w,a}, \bar{v}_{w,a}, \bar{p}_{w,a})$ the axial, radial and pressure perturbations for the water (w) and air (a) respectively, both the continuity and axial momentum equation for the gas stream read,

$$\frac{\partial \bar{u}_a}{\partial z} + \frac{1}{r}\frac{\partial (r\bar{v}_a)}{\partial r} = 0, \tag{5.1}$$

$$\rho_a \left(\frac{\partial \bar{u}_a}{\partial t} + (U_a - U_w)\frac{\partial \bar{u}_a}{\partial z} \right) = -\frac{\partial \bar{p}_a}{\partial z}, \tag{5.2}$$

where z and r are the axial and radial cylindrical coordinates, respectively. On the other hand, the kinematic condition at the interface states that

$$\frac{\partial f}{\partial t} + (U_a - U_w)\frac{\partial f}{\partial z} = \bar{v}_a \quad \text{at } r = r_o, \tag{5.3}$$

where $r = r_o + f$ is the location of the free surface. Taking into account that in the limit $kr_o \ll 1$, in the first approximation, the fluctuating air velocity only depends on z, $\bar{u}_a \simeq \bar{u}_a(z)$, and integrating the continuity equation, (5.1), between $r = 0$ and $r = r_o$, we obtain

$$\frac{\partial \bar{u}_a}{\partial z} = -2\left(\frac{\partial (f/r_o)}{\partial t} + (U_a - U_w)\frac{\partial (f/r_o)}{\partial z} \right). \tag{5.4}$$

Seeking for solutions of the form $(\bar{u}_{w,a}, \bar{v}_{w,a}, \bar{p}_{w,a}, f) = (u_{w,a}, v_{w,a}, p_{w,a}, F)$ $\exp(\mathrm{i}(kz - \Omega t))$ and introducing (5.4) into (5.2), we obtain

$$p_a = 2\rho_a (U_a - U_w)^2 \left[\frac{\Omega}{(U_a - U_w)k} - 1 \right]^2 \frac{F}{r_o}. \tag{5.5}$$

Furthermore, the normal stress jump condition across the interface provides the liquid pressure at the interface,

$$p_w \simeq p_a + \frac{F}{r_o}\frac{\sigma}{r_o} = 2\rho_a (U_a - U_w)^2 \left[\frac{\Omega}{(U_a - U_w)k} - 1 \right]^2 \frac{F}{r_o} + \frac{F}{r_o}\frac{\sigma}{r_o}, \tag{5.6}$$

with errors of the order of $O \sim (k r_o)^2$.

On the other hand, the equations governing the perturbations in the water stream (moving in a frame of reference at the liquid velocity), under the assumption $kr_o \ll 1$, are simply

$$\frac{1}{r}\frac{\partial(r\bar{v}_w)}{\partial r} \simeq 0 \rightarrow \bar{v}_w = \frac{\bar{v}_w(r = r_o)\, r_o}{r}, \tag{5.7}$$

$$\rho_w \frac{\partial \bar{v}_w}{\partial t} = -\frac{\partial \bar{p}_w}{\partial r}, \tag{5.8}$$

with the following free-surface condition,

$$\bar{v}_w(r = r_o) = \frac{\partial f}{\partial t}. \tag{5.9}$$

Finally, the following dispersion relation can be obtained integrating the radial momentum equation, (5.8), between $r = r_o$ and $r = r_w$ and using (5.6) and (5.9),

$$-\Omega^2 = \rho_a (U_a - U_w)^2 / (\rho_w r_o^2 \ln(r_w/r_o)) \left[2 \left(\frac{\Omega}{(U_a - U_w)k} - 1 \right)^2 + We^{-1} \right]. \tag{5.10}$$

Note that, the frequency scaling obtained with a linear stability analysis under the assumption of quasi-steady flow, $\Omega/(k(U_a - U_w)) \ll 1$, is exactly the same as that provided in § 4 for the ligament collapse stage.

REFERENCES

Bhunia, A., Pais, S. C., Komotani, Y. & Kim, I. H. 1998 Bubble formation in a coflow configuration in normal and reduced gravity. *AIChE J.* **44**, 1499–1509.

Chuang, S. C. & Goldschmidt, V. W. 1970 Bubble formation due to a submerged capillary tube in quiescent and coflowing streams. *Trans. ASME* D: *J. Basic Engng* **92**, 705–711.

Gibson, L. J. & Ashby, M. F. 1999 *Cellular Solids: Structure and Properties*. Cambridge University Press.

Gordillo, J. M., Gañán Calvo, A. M. & Pérez-Saborid, M. 2001 Monodisperse microbubbling: absolute instabilities in coflowing gas–liquid jets. *Phys. Fluids* **13**, 3839–3842.

Kalaaji, A., Lopez, B., Attane, P. & Soucemarianadin, A. 2003 Breakup length of forced liquid jets. *Phys. Fluids* **15**, 2469–2479.

Kendall, J. M. 1986 Experiments on annular liquid jet instability and on the formation of liquid shells. *Phys. Fluids* **29**, 2086–2094.

Kumar, R. & Kuloor, N. R. 1970 The formation of bubbles and drops. *Adv. Chem. Engng* **8**, 256–368.

Monkewitz, P. A. & Sohn, K. D. 1988 Absolute instability in hot jets. *AIAA J.* **28**, 911–916.

Oğuz, H. & Prosperetti, A. 1993 Dynamics of bubble growth and detachment from a needle. *J. Fluid Mech.* **257**, 111–145.

Parthasarathy, R. N. & Chiang, K.-M. 1998 Temporal instability of gas jets injected in viscous liquids to three-dimensional disturbances. *Phys. Fluids* **10**, 2105–2107.

Sevilla, A., Gordillo, J. M. & Martínez-Bazán, C. 2002 The effect of the diameter ratio on the absolute and convective instability of free coflowing jets. *Phys. Fluids* **14**, 3028–3038.

Sevilla, A., Gordillo, J. M. & Martínez-Bazán, C. 2005 Transition from bubbling to jetting in a co-axial air-water jet. *Phys. Fluids* **17**, 018105.